JOURNAL OF PROPULSION AND POWER
Vol. 13, No. 3, May–June 1997

Skin-Friction Predictions in a Crossing-Shock Turbulent Interaction

Datta Gaitonde* and J. S. Shang†
U.S. Air Force Wright Laboratory, Wright–Patterson Air Force Base, Ohio 45433-7913

This work addresses some difficulties in the computation of skin-friction loads caused by shock wave/turbulent boundary-layer interactions in high-speed inlets. Of particular interest is the accuracy of k-ε based models for C_f prediction in the separated three-dimensional flowfield induced by a symmetric double-fin geometry at Mach 4. A compressibility correction and two length-scale limiting procedures are investigated. A strong correlation is observed between coherent trends in C_f and the flowfield structure near the surface. On the symmetry plane, all modifications improve predictions over the baseline model, but only in the initial interaction region. The downstream flow exhibits high gradients and manifests a central line of three-dimensional attachment straddled by longitudinal vortices. This physical complexity results in uniformly poor predictions. Off the symmetry plane, however, the flow features are relatively simpler, and remarkably good agreement is observed with experiment, particularly with the application of a compressibility correction. Some C_f trend discrepancies between experiment and computation are shown to be associated with a displaced development of mean structures in the computations.

Nomenclature

A_μ = constant in Rodi–Horstman model
C_f = skin-friction coefficient
$C_{\varepsilon 1}$ = turbulence model constant, 1.44
$C_{\varepsilon 2}$ = turbulence model constant, 1.92
C_μ = turbulence model constant, 0.09
D = low Reynolds number term for turbulence kinetic energy equation
E_ε = low Reynolds number term for turbulence energy dissipation equation
$\boldsymbol{F}_{k\varepsilon}, \boldsymbol{G}_{k\varepsilon}, \boldsymbol{H}_{k\varepsilon}$ = vector fluxes for k-ε equations
$f_{\varepsilon 2}$ = function in source term, $\boldsymbol{S}$
f_μ = function in eddy viscosity definition
J = Jacobian of coordinate transformation
k = turbulence kinetic energy
l = turbulent length scale
M_∞ = freestream Mach number
P_k = turbulence production source term
Pr = Prandtl number, 0.73 for air
Pr_t = turbulent Prandtl number, 0.90
Re = reference Reynolds number
Re_t = Reynolds number of turbulence
Re_y = Reynolds number based on y
$\boldsymbol{S}$ = vector source term
T = temperature
U = contravariant velocity component
$\boldsymbol{U}_{k\varepsilon}$ = vector of dependent variables in k-ε equations
u_i = Cartesian velocity components
x_i = Cartesian coordinates, x, y, z
α = compressibility correction coefficient
ε = turbulence energy dissipation
μ, μ_t = molecular and turbulent viscosity coefficients
ξ, η, ζ = computational coordinates
ξ_i = computational coordinates, ξ, η, ζ
ρ = nondimensional fluid density
σ_k = turbulence model constant, 1.0
σ_ε = turbulence model constant, 1.3
τ_{ij} = components of viscous stress tensor

I. Introduction

ONE of the principal phenomena affecting the design of supersonic inlets is the interaction of shock waves with boundary layers. In ramjets and scramjets such interactions are an essential consequence of flow compression and deceleration required prior to combustion. Under typical conditions, three-dimensional separation occurs with the formation of vortical structures. This adversely affects pressure recovery and distortion and degrades propulsion system performance. Additionally, severe mechanical and thermal loads are produced that must be accounted for in an efficient design methodology to prevent catastrophic failure. The development of prediction methods for, and understanding of, shock-wave/turbulent boundary-layer interaction should greatly impact high-speed aircraft design.

In recent years, synergism between experimental and computational efforts has contributed significantly to the understanding of turbulent interactions. The configurations considered are simple, consisting usually of a plate-mounted shock generator. One of the most extensively examined situations is the single-fin (SF) configuration consisting of a wedge mounted on a plate. An excellent description of this flowfield is found in Ref. 1. The present work focuses, however, on the interaction caused by the double-fin geometry (DF), shown in Fig. 1. Two opposed symmetric fins, separated by a finite distance, are mounted on a flat plate. The flow parameters of interest include the Mach and Reynolds numbers, the properties of the incoming boundary layer, the fin angles, the distance between the fins, and the wall thermal conditions. This flowfield has also received significant attention in the last 10 years.[2–7]

Despite computer speed enhancements, direct numerical simulation of turbulent flows is not yet feasible for these conditions. Because of turbulence modeling uncertainties, a critical component of simulation is the comparison with experi-

---

Presented as Paper 96-0043 at the AIAA 34th Aerospace Sciences Meeting, Reno, NV, Jan. 15–19, 1996; received Aug. 8, 1996; revision received Jan. 22, 1997; accepted for publication Jan. 28, 1997. This paper is declared a work of the U.S. Government and is not subject to copyright protection in the United States.

*OAI/COMP, Visiting Scientist, WL/FIMC, Building 450, 2645 Fifth Street, Suite 7, E-mail: datta@fim.wpafb.af.mil. Senior Member AIAA.

†Senior Scientist, WL/FIMC, Building 450, 2645 Fifth Street, Suite 7. Fellow AIAA.

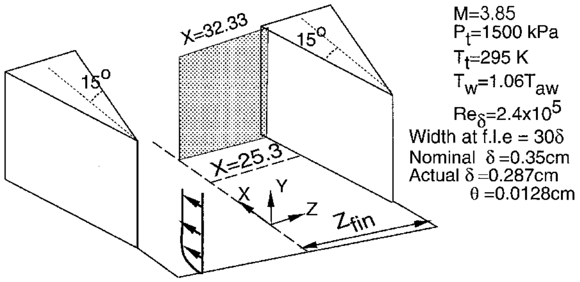

Fig. 1 DF geometry and flow parameters.

mental data. Several quantities have been measured in the double-fin flow at various Mach and Reynolds numbers. Quantitative measurements include surface pressures, C_f, heat transfer rates, and pitot pressure surveys. Flow visualization measurements include surface oil flow patterns and planar laser scattering (PLS) images of shock structure.

Comparison of computations with experiment indicates good agreement for all of the previous quantities with the prominent exception of skin-friction coefficients[5,6] and heat transfer rates,[4,7] both of which are evaluated with wall gradients. These discrepancies have generally been attributed to turbulence modeling.[4–7] In recent years several modifications have been proposed in the context of two-dimensional interactions to deal with the phenomena associated with supersonic compressible separated flows (see Ref. 8 for a comprehensive list). Distinct corrections address complexities associated with adverse/favorable pressure gradients, separation, and compressibility. The DF flow contains many of these features. However, corrections to the turbulence model must be examined with care since they may degrade performance in benign regions of the flow.[9]

Our objectives in this work may be stated as follows:

1) In Sec. III, we characterize the deficiency in the performance of the baseline Jones–Launder model.[10,11] The experimental data chosen for model evaluation purposes were obtained by Garrison et al.[5] Figure 1 summarizes the flow parameters.

2) In Sec. IV, we first outline the flowfield structure originally described in Refs. 6 and 7. We then employ this understanding of the coherent features to select three relatively simple but popular turbulence model modifications anticipated to have a significant impact on the accuracy of the computations. These three modifications are, respectively, the compressibility correction of Sarkar et al.,[12] the length-scale modification of Vuong and Coakley,[13] and the two-layer model of Rodi[14] in the form implemented by Horstman.[15]

3) In Sec. V, we investigate the performance of these modifications and correlate our observations to the flowfield structure.

II. Theoretical Model

The three-dimensional compressible Navier–Stokes equations are solved in strong conservation form and mass-averaged variables in a curvilinear coordinate system. Details of the numerical algorithm may be found in Refs. 16–18. The inviscid fluxes are evaluated with Roe's flux-difference split scheme.[19] Third-order accuracy is obtained with the MUSCL approach[20] in conjunction with a harmonic limiter for monotonicity. Viscous terms are differenced to second-order accuracy in a centered manner. The molecular viscosity μ is evaluated with Sutherland's law. The effects of turbulence are incorporated through the μ_t assumption, and the turbulent Prandtl number is assumed constant at 0.9.

The baseline turbulence model is the k-ε formulation with low Reynolds number terms.[10,11] A brief description of this method is presented. In flux vector form, the governing equations for the k-ε equations are written in general curvilinear coordinates (ξ, η, ζ) as

$$\frac{\partial \boldsymbol{U}_{k\varepsilon}}{\partial t} + \frac{\partial \boldsymbol{F}_{k\varepsilon}}{\partial \xi} + \frac{\partial \boldsymbol{G}_{k\varepsilon}}{\partial \eta} + \frac{\partial \boldsymbol{H}_{k\varepsilon}}{\partial \zeta} = S \tag{1}$$

where

$$\boldsymbol{U}_{k\varepsilon} = \frac{1}{J}\begin{bmatrix} \rho k \\ \rho\varepsilon \end{bmatrix} \tag{2}$$

$$\boldsymbol{F}_{k\varepsilon} = \frac{1}{J}\begin{bmatrix} \rho k U - \left(\mu + \dfrac{\mu_t}{\sigma_k}\right) \xi_{x_i} \dfrac{\partial \xi_j}{\partial x_i} \dfrac{\partial k}{\partial \xi_j} \\[2ex] \rho \varepsilon U - \left(\mu + \dfrac{\mu_t}{\sigma_\varepsilon}\right) \xi_{x_i} \dfrac{\partial \xi_j}{\partial x_i} \dfrac{\partial \varepsilon}{\partial \xi_j} \end{bmatrix} \tag{3}$$

Similar formulas may be written for $\boldsymbol{G}_{k\varepsilon}$ and $\boldsymbol{H}_{k\varepsilon}$. The vector source term is written as

$$\boldsymbol{S} = \frac{1}{J}\begin{bmatrix} -(P_k - \rho\varepsilon + D) \\ -(C_{\varepsilon 1} P_k \varepsilon / k - C_{\varepsilon 2} f_{\varepsilon 2} \rho \varepsilon^2 / k + E_\varepsilon) \end{bmatrix} \tag{4}$$

The various terms in the previous equations are

$$\mu_t = C_\mu f_\mu Re_t \mu, \qquad Re_t = Re(\rho k^2/\mu\varepsilon) \tag{5}$$

$$D = -\frac{2\mu}{Re} \sum_i \left(\frac{\partial \xi_j}{\partial x_i} \frac{\partial k^{1/2}}{\partial \xi_j}\right)^2, \qquad P_k = \frac{1}{Re} \tau_{t_{ij}} \frac{\partial \xi_k}{\partial x_j} \frac{\partial u_i}{\partial \xi_k} \tag{6}$$

$$\tau_{t_{ij}} = \mu_t \left(\frac{\partial \xi_k}{\partial x_j} \frac{\partial u_i}{\partial \xi_k} + \frac{\partial \xi_k}{\partial x_i} \frac{\partial u_j}{\partial \xi_k} - \frac{2}{3} \delta_{ij} \frac{\partial \xi_l}{\partial x_k} \frac{\partial u_k}{\partial \xi_l}\right) \tag{7}$$

$$E_\varepsilon = \frac{2\mu\mu_t}{\rho Re^2} \sum_i \left(\frac{\partial \xi_k}{\partial x_j} \frac{\partial \xi_l}{\partial x_j} \frac{\partial^2 u_i}{\partial \xi_k \partial \xi_l}\right)^2 \tag{8}$$

$$f_\mu = \exp\left[\frac{-3.4}{(1 + 0.02 Re_t)^2}\right] \qquad f_{\varepsilon 2} = 1 - 0.3 \exp(-Re_t^2) \tag{9}$$

$$C_\mu = 0.09, \quad C_{\varepsilon 1} = 1.44, \quad C_{\varepsilon 2} = 1.92 \qquad \sigma_k = 1.0, \quad \sigma_\varepsilon = 1.3 \tag{10}$$

The boundary conditions are summarized as follows: on solid surfaces the no-slip condition is enforced, the wall temperature is specified based on experimental data ($T_{\text{wall}} = 1.06 T_{\text{adiabatic}}$), and the normal pressure gradient, k and ε, are all assumed zero. The incoming boundary-layer profile is specified at a distance 4δ upstream of the fin leading edges (f.l.e), by matching the momentum thickness ($\theta = 0.128$ mm at the f.l.e) with two-dimensional calculations. The downstream and top boundaries are assumed to be far enough away for the application of simple zero-gradient extrapolation. Symmetry conditions are applied on two planes, one upstream of the f.l.e ($Z = Z_{\text{fin}}$ in Fig. 1) and the other equidistant between the two fins ($Z = 0$). In the text, the term symmetry plane refers to the latter.

The grid is generated as a sequence of nonuniform Cartesian planes normal to the direction of the upstream flow. The clustering process addresses issues of viscous sublayer and boundary layer as well as streamwise and crossflow resolution. For

Table 1 Grid size and mean spatial resolution

Mesh	$IL^a \times JL^b \times KL^c$	$\Delta x/\delta$	$\Delta y/\delta$	$\Delta z/\delta$	y^{+d}
$M1$	99 × 88 × 114	0.45	0.16	0.10	1.00
$M2$	119 × 121 × 135	0.34	0.12	0.07	0.7

[a] IL = Number of points in ξ direction.
[b] JL = Number of points in η direction.
[c] KL = Number of points in ζ direction.
[d] y^+, height of first point away from plate in wall units at upstream boundary.

evaluating grid dependence, results are described on two meshes, denoted $M1$ and $M2$, respectively, with the properties summarized in Table 1. $M1$ consists of roughly 1 million points and extends beyond the fin trailing edge where a duct is appended, whereas $M2$ with about 2 million points terminates at the trailing edge of the fin. Convergence is ascertained by monitoring several quantities including the global norm, surface pressure, and skin-friction coefficients.

III. Performance of Baseline Turbulence Model

First, the numerical issue of mesh adequacy is addressed. Then the deficiencies of the baseline model are characterized by comparison with experimental C_f data. The correlation of the observed trends with flow structure is deferred to Sec. V.

Figure 2 displays the pressures at the two surface locations shown in Fig. 1: a spanwise cut at a streamwise distance $X = x/\delta = 25.3$, where δ is the nominal boundary-layer thickness ($\delta = 3.5$ mm), and a streamwise cut along the symmetry plane $Z = z/\delta = 0$. There is no significant sensitivity to mesh resolution at this level of refinement at either location. Although no experimental surface pressure data are available for this channel width, previous comparisons[6] show reasonably good agreement for a slightly narrower channel. A crude measure of validation may be achieved by noting that in the vicinity of each fin leading edge, but outside of an inception zone, the present flow constitutes a single-fin interaction whose surface features are conical and for which a large number of parametric studies exist. The computed results indicate that the angle formed by the ray of upstream influence, determined by an initial pressure rise of 0.5% over its upstream value, with the freestream direction to be approximately 38 deg, which compares well with the experimental single-fin data of Ref. 21 for similar Mach and Reynolds numbers. The solution is also effectively mesh independent for field values: Fig. 3 displays computed pitot pressures at the crossflow plane $X = 32.33$, which is depicted schematically in Fig. 1. The dominant feature consists of a large inverted heart-shaped low pitot-pressure region whose features are nearly identical on both meshes. Like surface pressure, the flow surveys have shown excellent agreement with experimental observations at present[6] and higher[4,7] Mach numbers.

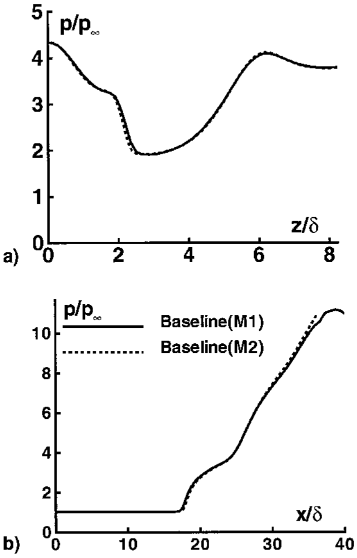

Fig. 2 Effect of mesh resolution on surface pressure with baseline model on a) $X = 25.3$ crossflow plane and b) symmetry plane $Z = 0$.

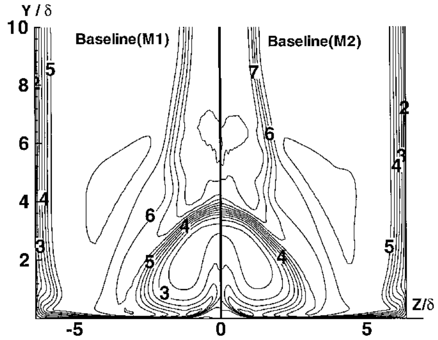

Fig. 3 Pitot pressure (normalized by freestream total pressure) variation with mesh resolution. Level increment is 0.07 starting with 0.0 at level 1.

The comparison of skin-friction with experimental data on the crossflow plane is exhibited in Fig. 4. Ten percent uncertainty is marked on the experimental data as specified in Ref. 5. The solution displays more mesh sensitivity to skin-friction values than to pressure. The mean change upon doubling the mesh is still less than 4%, which is considerably lower than the uncertainty bound of the experimental data. Experimental C_f data exhibit a rapid rise near the fin ($Z \sim 8$) to reach a maximum near $Z \sim 6$. Proceeding toward the symmetry plane, a W-shaped profile is perceptible, as highlighted in Fig. 4. Local minima near $Z \sim 2.75$ (A in Fig. 4) and $Z \sim 1$ (C in Fig. 4) alternate with local maxima at $Z \sim 2$ (B in Fig. 4) and $Z \sim 0$ (D in Fig. 4). Although the experimental data measurements are sparse in this region, the experimentalists note that these trends cannot be attributed to data scatter since they are confirmed by oil fringe distributions.[5] The computed results follow the trends of experimental data in the region $4 < Z < 8.2$ with modest overprediction. However, significant discrepancies are observed in the area of the symmetry plane. The computed rapid rise in C_f values near $Z \sim 2$ may be correlated with that in experiment near $Z \sim 2.5$ (between A and B in Fig. 4), but it is clear that the baseline simulations do not predict either the magnitudes or even the trends satisfactorily in this region.

C_f values on the symmetry plane are plotted in Fig. 5. Good agreement is obtained in the upstream boundary layer. Experimental skin friction values show a decline significantly

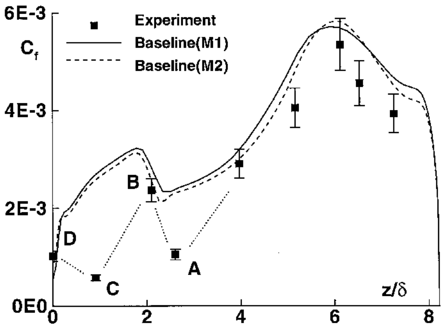

Fig. 4 Baseline model C_f prediction on spanwise plane, $X = 25.3$.

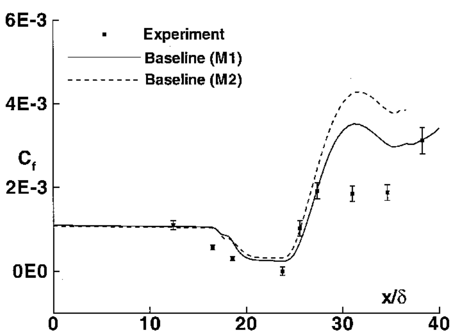

Fig. 5 Baseline model C_f prediction on symmetry plane, $Z = 0$.

prior to and greater than computations. The experimental skin-friction then goes to zero, indicating separation of the boundary layer on the symmetry plane.[5] The computed values, however, remain positive with the finer mesh producing even larger values. The subsequent rapid recovery of the C_f profile is predicted quite well on both meshes. Further downstream, the experimental data reach a plateau, however, while the computed values on both meshes increase monotonically up to $X = 30\delta$. Perhaps more significantly, even though surface pressure (Fig. 2) shows mesh convergence, C_f varies on the two meshes by as much as 35% in the downstream regions with the finer mesh predicting values in greater error. Further mesh enrichment studies do not show the potential for increased accuracy since results on $M2$ show greater deviation from experiment than $M1$. Detailed examination reveals that the solution displays unacceptably high mesh dependence of C_f only in the immediate vicinity adjacent to the symmetry plane.

In summary, the baseline model exhibits significant inaccuracies in C_f prediction. On the spanwise plane, C_f values show relative mesh independence, but differ from experiment, particularly near the symmetry plane. On the symmetry plane itself, the absence of a reversed flow region contradicts the experimental observations of Ref. 5, whereas downstream, the method has not converged on meshes that are rather fine by contemporary standards for such interactions and domain sizes. Local grid resolution criteria are highly dependent upon the local flow structure. It will be demonstrated that the region near the symmetry plane is dominated by secondary features.

IV. Turbulence Model Modifications

Several modifications have been suggested to the baseline model.[8] To focus on those most relevant to these computations, we rely on an understanding of the flow structure. For completeness, the salient features of the description originally presented in Refs. 6 and 7 are outlined. Reasonable confidence may be placed on this qualitative description because measurements related to large-scale features such as field pitot surveys, surface oil flow, and shock structure show excellent agreement with experiment and are further relatively insensitive to the turbulence model.[6] Figure 6 divides the field into four coherent structures. Note that the axes have been rescaled for clarity. The incoming boundary layer (BL) separates from the plate and does not reattach. This surface becomes narrow downstream and rolls around to form a scroll-like structure in cross section straddling the symmetry plane. Fluid attaching near the corner sweeps spanwise beneath the separating boundary layer. The vortex interaction regime (VI) forms a shear layer with the separated boundary layer. The entrainment flow (EF) originates in the outer region. After attachment, a new boundary layer forms, sweeps across the channel, and separates prior to reaching the centerline. Two mirror counterparts of a centerline vortex (CV) straddle the symmetry plane.

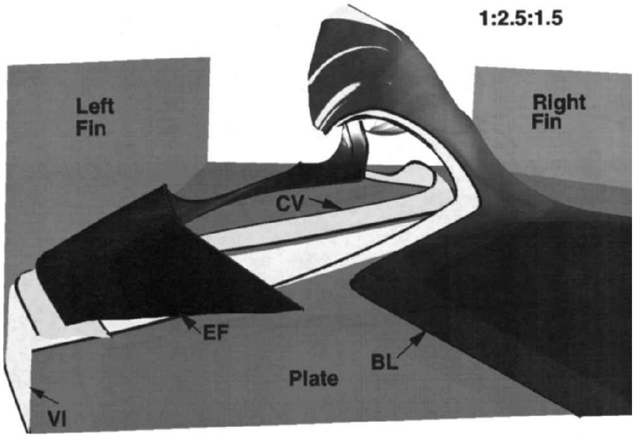

Fig. 6 Streamline structure.

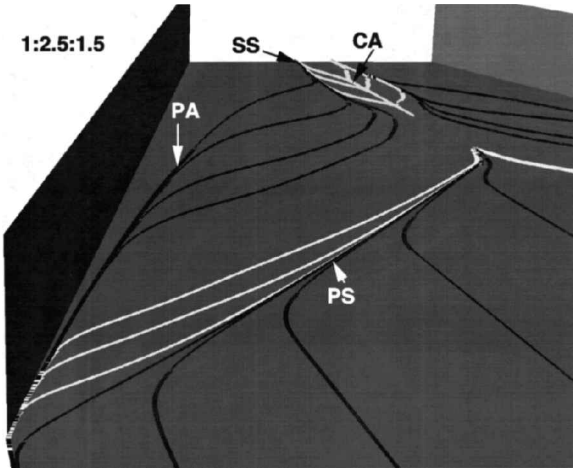

Fig. 7 Surface oil-flow structure.

The surface streamline pattern is shown in Fig. 7. Four distinct lines of coalescence/divergence are readily evident. The incoming fluid forms a line of coalescence denoted the primary line of separation (PS). A line of attachment forms near each fin–plate corner (PA). Near the center of the channel, two secondary lines of separation (SS) straddle a centerline of attachment (CA) on the symmetry plane. This pattern bears good resemblance to the principal features noted in the experiment of Ref. 22, as has been shown in Ref. 6.

This description suggests the suitability of several enhancements to the baseline model.

A. Compressibility Correction (CC)[12]

Computations of supersonic shear layers, separation, and attachment are known to benefit from the incorporation of explicit compressibility corrections beyond the assumption of variable mean density.[9] The first correction examined accounts for compressibility effects with the formula of Sarkar et al.[12] In this, the source term for k in Eq. (4) is modified to read:

$$S = \frac{1}{J}\begin{bmatrix} -[P_k - \rho\varepsilon(1 + M_t^2) + D] \\ -(C_{\varepsilon 1}P_k\varepsilon/k - C_{\varepsilon 2}f_{\varepsilon 2}\rho\varepsilon^2/k + E_\varepsilon) \end{bmatrix}$$

where $M_t^2 = 2M_\infty^2 k/T$.

B. Two-Layer Models

In regions removed from the vicinity of the symmetry plane, the flowfield near the plate is dominated by the crossflow development of the entrainment flow subsequent to attachment. It is well known (see Ref. 8 and references therein) in the context of postattachment two-dimensional/axisymmetric situations that the baseline k-ε model suffers from the phenomenon of an abnormal collapse of ε near (re)attachment and leads to a strong growth in turbulent length-scale. Limiting of the length-scale near the surface results in a two-layer model. We focus on two of the several methods described in the literature:

1. *Method of Vuong and Coakley[13] (VC)*

The length-scale l is restricted by the vertical distance from the surface y:

$$l = \min[2.5y, (\sqrt{k^3}/\varepsilon)] \qquad \varepsilon = \sqrt{k^3}/l \tag{11}$$

This restriction is applied only to the plate boundary layer.

2. *Method of Rodi[14] as Implemented by Horstman[15] (RH)*

A second method of length-scale specification is attributed to Rodi[14]; the particular form employed here was used by Horstman[15] for compressible two-dimensional and axisymmet-

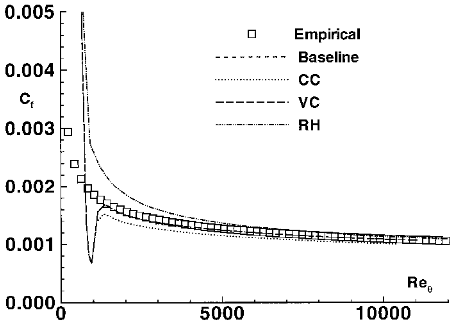

Fig. 8 Comparison of models in upstream boundary layer. Empirical results of Sommer and Short.[23]

ric flows. The eddy viscosity in the near-wall region is determined from the relation:

$$\mu_t = f_\mu C_\mu \rho\sqrt{k}\,l \tag{12}$$

where $f_\mu = 1 - e^{-Re_y/A_\mu}$, $A_\mu = 70$, $Re_y = \rho\sqrt{k}y/\mu$, and $l = 2.5y$. This relationship is applied on both the fin and the plate boundary layers at points where $f_\mu < 0.95$. At these points, the dissipation rate is then redefined as

$$\varepsilon = \frac{k^{3/2}}{l}\left[1 + \frac{13.2}{(\rho\sqrt{k}l/\mu)}\right] \tag{13}$$

For consistency with the original formulation, both $f_{\varepsilon 2}$ and f_μ are set to unity, the latter function is only outside of the region where the length-scale is specified.

The implementation of the modifications is verified for the upstream two-dimensional boundary-layer computation. Figure 8 compares C_f values obtained with the various models. Except near the leading edge, all models predict values to within 10% of the empirical correlation of Sommer and Short.[23] Although not shown, these results are not sensitive to increased mesh resolution. The compressibility correction of Ref. 12 lowers C_f values by roughly 8% in the region of interest. This is consistent with the findings of Refs. 8 and 9 for wall-bounded shear layers and is attributed to an effective lowering of κ.[9] Despite this shortcoming in the upstream region, the compressibility correction is known to be beneficial in separated shear layers.[9] Interestingly, the VC model results are identical to those of the baseline model because the condition of Eq. (11) is not triggered in the upstream flat-plate boundary layer. Finally, the RH model also reaches excellent agreement with the data when the value of A_μ is adjusted to 70. Comparison of the near-wall profiles (not shown) with the effective velocity approach of van Driest shows similarly good agreement with the law of the wall. It is relevant to mention here that in Ref. 5 the RH model has been employed on a nominally similar configuration. However, a direct comparison with that effort is not pursued since in addition to the value of A_μ, material differences exist in other aspects of the numerical algorithm, mesh density, and configuration.

V. Performance of Modified Models in Interaction Region

The effect of the previous model modifications on surface pressures is relatively minor. Although not shown for brevity, the compressibility correction has a modest positive impact on the computation of pitot pressure: the height of the region of low pitot pressure is more accurately predicted. In contrast, the two length-scale limited methods do not show any deviation from the baseline model in this regard.

Turning to the more critical C_f prediction, Fig. 9 compares the performance of the different models at the $X = 25.3$ spanwise section. Calculations with the RH model show negligible differences on the two meshes. Mesh resolution requirements are lower for this two-layer model because of the effective absence of some low Reynolds number terms.[14] Both the CC and RH modifications lower C_f values in regions removed from the symmetry plane, bringing a much closer agreement with the experiment. In fact, the compressibility correction predicts C_f values within the experimental scatter for a large part of the channel. Overall, the VC modification shows the least deviation from the baseline model in this plane. None of the models improves predictions over the baseline model near the symmetry plane at this spanwise section: the W-shaped profile is not obtained. This aspect is analyzed in greater detail later.

C_f results on the symmetry plane are shown in Fig. 10. Excluding the trailing end of the domain, again only minor differences are evident with the RH model on the two meshes. The onset of C_f drop varies significantly with the model. The most accurate result is obtained with the compressibility correction. More crucially, all modifications predict the separation of the incoming boundary layer on the symmetry plane, noted in the negative C_f values, as observed in experiment.[5] The rise in C_f subsequent to attachment ($X \sim 24$) is most rapid with CC, which also shows the largest overprediction of skin-friction. Both length-scale modifications predict downstream movement of the point of attachment and subsequent C_f recovery. This observation is consistent with the two-dimensional results of Ref. 8 where length-scale modifications were observed to retard reattachment points in supersonic flows as opposed to hypersonic regimes where the predictions are better. Only the RH model shows a relatively rapid leveling off of C_f, but the plateau is reached at a considerably higher level and is displaced downstream of the experimental location.

The large discrepancies on the symmetry plane may be attributed to the behavior of the turbulence model in the complex three-dimensional flow in the immediate vicinity of this plane. This hypothesis is consistent with both the high sensitivity of the baseline model to the mesh and the fact that all tested models fail to reproduce C_f data accurately. As noted in Fig. 7, the entire symmetry line in the downstream region is one of three-dimensional attachment (CA), a phenomenon difficult to model even in two-dimensional situations, where models are

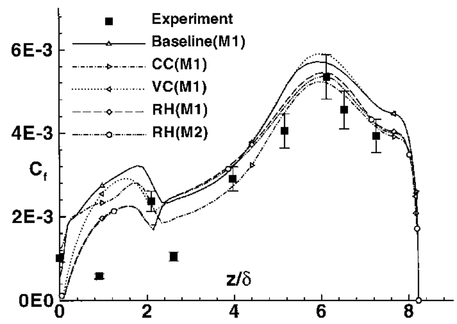

Fig. 9 Performance of modified models: C_f comparison on spanwise plane, $X = 25.3$.

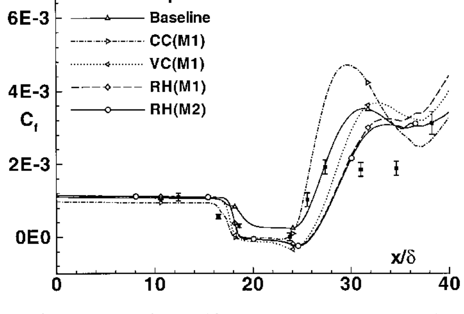

Fig. 10 Performance of modified models: C_f comparison on symmetry plane, $Z = 0$.

typically calibrated. The inherently three-dimensional characteristic of the flow at the symmetry plane may be recognized from the fact that the separating streamline does not reattach, the downstream zero C_f location being associated with attachment of the flow approaching the symmetry plane from the sides as discussed in Ref. 6. The symmetry plane is further straddled by the relatively small longitudinal vortices, CV, as shown in Fig. 6. While these vortices have not directly been observed in experiment, their existence is consistent with the observed surface oil flow pattern that shows a distinct centerline of attachment straddled by two lines of separation.[5]

Given the fact that the principal flow features are captured, the following questions arise: what is the significance of the W-shaped profile in Fig. 4, and why is it absent in the calculations? To investigate this, Fig. 11 presents the experimental C_f at $X = 25.3$ and the computed CC results at $X = 25.3$ and 27.8. The latter section is chosen at a position where the same W sequence of local maxima and minima observed in the experiment (points A–D in Fig. 11) is highlighted in the computation (A_c, B_c, C_c, and D_c). The C_f development is very similar near the fin at the two computational stations plotted. This is indicative of the similar development of the entrainment flow after attachment at various downstream locations. Because of this it is possible to propose a correlation of the W pattern in the crossflow data with the sequence of physical processes encountered by a typical streamline, even though its streamwise velocity is nonzero. Details of the computed shock structure and comparison with experiment may be found in Ref. 6. A brief synopsis is shown in Fig. 12, which presents a view of the channel looking downstream. The pressure and magnitude of the three-dimensional pressure gradient $|\nabla p|$ are plotted on a spanwise plane at $X = 25.5$. All of the shocks noted in this figure have been identified in experimental PLS visualization.[22] Also displayed are velocity vectors along two plate-normal lines. Referring to the ribbon plot of Fig. 6, the entrainment flow, after attaching near the fin–plate junction, sweeps spanwise toward the symmetry plane and initially experiences an overall favorable pressure gradient. This forms a skewed wall-jet-like structure that is clearly evident in Fig. 12 and is accompanied by a drop in C_f values. For single fins, even relaminarization of this regime has been observed.[24] In its trajectory toward the symmetry plane, this jet then encounters two distinct regions of adverse pressure gradient. The first is a consequence of the system of shocks reflected from the symmetry plane, the foot of the reflected separation shock (RSS).[6] This rapid rise is also noted in Fig. 2 at $Z \sim 2.5$. This interaction does not cause separation but is accompanied by an initial decline in C_f (point A in Fig. 11) followed by strong recovery to reach a maximum at point B. These trends are consistent with those experienced by an unseparated boundary layer undergoing rapid compression. For example, experimental results show similar C_f variation on unseparated two-dimensional compression corner turbulent interactions.[25] The base of the reflected separation shock does not fully align the jet parallel to the symmetry plane. It then impinges on the symmetry plane at an oblique angle resulting in a stagnation-like process causing a second pressure rise associated with a plate center-line shock (PCS), as shown in Fig. 12. This causes a second decline in C_f and ultimately leads to separation associated with SS whose location is marked in Fig. 11. Interestingly, secondary separation does not coincide with the local minimum C_c. The value of C_f at point C_c is not easily correlated with the physics since the region between SS and the symmetry plane is occupied by the centerline vortices whose behavior is strongly dependent upon local features outside of the crossflow plane under study. We note, however, that the centerline is itself a line of attachment, CA, and exhibits local C_f (Fig. 11) and p (Fig. 2) maxima.

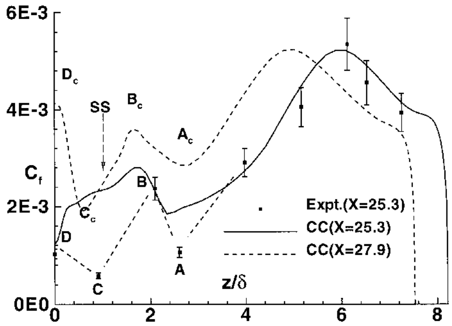

Fig. 11 C_f **plot with compressibility correction showing development of W structure.**

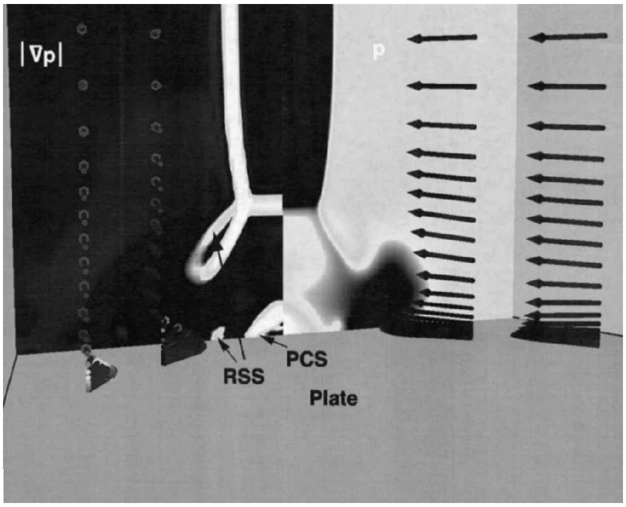

Fig. 12 Shock and streamline structure.

In a strict sense, such complex three-dimensional flows cannot be modeled by the eddy viscosity formulation that imposes a close relationship between the laminar and turbulent stress tensors. In addition to the inability to reproduce the inherent unsteadiness in the interaction (e.g., Refs. 26 and 27), it is noted further in Ref. 28 that "turbulence models extrapolated from 2-D experience miss some essential features of 3-D flows." The previous analysis suggests strongly that centerline data are difficult to reproduce accurately because of the local dominance of secondary flow features of high physical complexity and three dimensionality. Models seeking to obtain quantitative details correctly for engineering purposes must account satisfactorily for the extra strain rates[29] of the secondary features. Given that the relevant features are obtained, there is hope that a recalibration of turbulence model may achieve this goal. However, since the details have no direct counterpart in two dimensionality, this is likely to be a computationally intensive endeavor.

VI. Conclusions

An investigation of several k-ε based turbulence modeling methods reveals significant discrepancies in centerline C_f predictions. The analysis suggests that this failure is caused by the presence of secondary features characterized by high gradients and three dimensionality near the centerline where the basic assumptions inherent in the eddy viscosity formulation fail. Even though the processes encountered by the entrainment flow are also complex, C_f values are computed accurately in the large portion of the channel, particularly with the CC and RH formulations. Some trend discrepancies in the crossflow plane are associated with delayed development of coherent features. Given the simplicity of the eddy viscosity approach, this is encouraging from an engineering standpoint. When taken with the good to excellent computation of nearly every other feature of the mean flow, the poor prediction of centerline C_f values may be viewed as an anomaly in the performance of the previous turbulence models.

Acknowledgments

This work was supported in part by a grant of High Performance Computing time from the Department of Defense HPC Shared Resource Center, Corps of Engineers Waterways Experiment Station, Vicksburg, Mississippi. The authors thank M. Visbal, M. Aftosmis, A. A. Zheltovodov, and P. G. Huang for enlightening discussions.

References

[1] Settles, G. S., and Dolling, D. S., "Swept Shock/Boundary-Layer Interactions: Tutorial and Update," AIAA Paper 90-0375, Jan. 1990.

[2] Mee, D., and Stalker, R., "Investigation of Weak Shock-Shock and Shock-Expansion Intersection in the Presence of a Turbulent Boundary Layer," AIAA Paper 87-0549, Jan. 1987.

[3] Gaitonde, D., and Knight, D., "Numerical Investigation of Some Control Methods for 3-D Turbulent Interactions Due to Sharp Fins," AIAA Paper 89-0360, Jan. 1989.

[4] Narayanswami, N., and Horstman, C. C., and Knight, D. D., "Computation of Crossing Shock/Turbulent Boundary Layer Interaction at Mach 8.3," *AIAA Journal*, Vol. 21, No. 8, 1993, pp. 1369–1376.

[5] Garrison, T. J., Settles, G. S., Narayanswami, N. N., and Knight, D. D., "Laser Interferometer Skin-Friction Measurements of Crossing-Shock-Wave/Turbulent-Boundary-Layer Interactions," *AIAA Journal*, Vol. 32, No. 6, 1994, pp. 1234–1241.

[6] Gaitonde, D., and Shang, J. S., "The Structure of a Double-Fin Turbulent Interaction at Mach 4," *AIAA Journal*, Vol. 33, No. 12, 1995, pp. 2250–2258; also AIAA Paper 94-2810, June 1994.

[7] Gaitonde, D., Shang, J. S., and Visbal, M. R., "Structure of a Double-Fin Turbulent Interaction at High Speed," *AIAA Journal*, Vol. 33, No. 2, 1995, pp. 193–200.

[8] Coakley, T. J., and Huang, P. G., "Turbulence Modeling for High Speed Flows," AIAA Paper 92-0436, Jan. 1992.

[9] Wilcox, D. C., "Progress in Hypersonic Turbulence Modeling," AIAA Paper 91-1785, June 1991.

[10] Jones, W. P., and Launder, B. E., "The Prediction of Laminarization with a Two-Equation Model of Turbulence," *International Journal of Heat and Mass Transfer*, Vol. 15, No. 2, 1972, pp. 301–314.

[11] Launder, B. E., and Sharma, B. I., "Application of the Energy Dissipation Model of Turbulence to the Calculation of Flows near a Spinning Disk," *Letters in Heat and Mass Transfer*, Vol. 1, 1974, pp. 131–138.

[12] Sarkar, S., Erlebacher, G., Hussaini, M. Y., and Kreiss, H. O., "The Analysis and Modelling of Dilational Terms in Compressible Turbulence," *Journal of Fluid Mechanics*, Vol. 227, 1991, pp. 473–493.

[13] Vuong, S. T., and Coakley, T. J., "Modeling of Turbulence for Hypersonic Flows with and Without Separation," AIAA Paper 87-0286, Jan. 1987.

[14] Rodi, W., "Experience with Two-Layer Models Combining the k-ε Model with a One-Equation Model near the Wall," AIAA Paper 91-0216, Jan. 1991.

[15] Horstman, C. C., "Hypersonic Shock-Wave Turbulent Boundary-Layer Interaction Flows—Experiment and Computation," AIAA Paper 91-1760, June 1991.

[16] Visbal, M. R., "Structure of Laminar Juncture Flows," *AIAA Journal*, Vol. 29, No. 8, 1991, pp. 1273–1282.

[17] Rizzetta, D. P., "Numerical Investigation of Supersonic Wing-Tip Vortices," AIAA Paper 95-2282, June 1995.

[18] Gaitonde, D., Edwards, J. R., and Shang, J. S., "The Computed Structure of a 3-D Turbulent Interaction Caused by a Cylinder/Offset Flare Juncture," AIAA Paper 95-0230, Jan. 1995.

[19] Roe, P. L., "Approximate Riemann Solvers, Parameter Vectors and Difference Schemes," *Journal of Computational Physics*, Vol. 43, No. 2, 1981, pp. 357–372.

[20] Van Leer, B., "Flux-Vector Splitting for the Euler Equations," Inst. for Computer Applications in Science and Engineering, Rept. 82-30, Sept. 1982.

[21] Lu, F. K., Settles, G. S., and Horstman, C. C., "Mach Number Effects on Conical Surface Features of Swept Shock-Wave/Boundary-Layer Interactions," *AIAA Journal*, Vol. 28, No. 1, 1990, pp. 91–97.

[22] Garrison, T. J., and Settles, G. S., "Interaction Strength and Model Geometry Effects on the Structure of Crossing-Shock Wave/Turbulent Boundary-Layer Interactions," AIAA Paper 93-0780, Jan. 1993.

[23] Sommer, S. C., and Short, B. J., "Free-Flight Measurements of Turbulent Boundary-Layer Skin Friction in the Presence of Severe Aerodynamic Heating at Mach Numbers from 2.8 to 7.0," *Journal of Aeronautical Sciences*, Vol. 23, No. 6, 1956, pp. 536–542.

[24] Zheltovodov, A. A., "Peculiarities of Development and Modeling Possibilities of Supersonic Turbulent Separated Flows," *Separated Flows and Jets*, edited by V. V. Kozlov and A. V. Dovgal, International Union of Theoretical and Applied Mechanics Symposium, Novosibirsk, Springer–Verlag, Berlin, 1990, pp. 225–236.

[25] Smits, A. J., and Muck, K.-C., "Experimental Study of Three Shock Wave/Turbulent Boundary Layer Interactions," *Journal of Fluid Mechanics*, Vol. 182, 1987, pp. 291–314.

[26] Tani, K., and Dolling, D. S., "Fluctuating Wall Pressures in a Mach 5 Crossing Shock/Turbulent Boundary Layer Interaction Including Asymmetric Effects," AIAA Paper 96-0045, Jan. 1996.

[27] Garg, S., and Settles, G. S., "Unsteady Pressure Loads Generated by Swept-Shock-Wave/Boundary-Layer Interactions," *AIAA Journal*, Vol. 34, No. 6, 1996, pp. 1174–1181.

[28] Bradshaw, P., "Progress in Turbulence Research," AIAA Paper 90-1480, June 1990.

[29] Bradshaw, P., "The Effect of Mean Compression or Dilatation on the Turbulence Structure of Supersonic Boundary Layers," *Journal of Fluid Mechanics*, Vol. 63, 1974, pp. 449–464.